

Physical Model of a MEMS Accelerometer for Low-g Motion Tracking Applications

Wei Tech Ang, Si Yi Khoo, Pradeep K. Khosla, and Cameron N. Riviere

*The Robotics Institute
Carnegie Mellon University
Pittsburgh, Pennsylvania 15213, USA*

techang@ri.cmu.edu, skhoo@andrew.cmu.edu, pkk@ece.cmu.edu & camr@ri.cmu.edu

Abstract – This paper develops a physical model of a MEMS capacitive accelerometer in order to use the accelerometer effectively in low-g motion tracking applications. The proposed physical model includes common physical parameters used to rate an accelerometer: scale factor, bias, and misalignment. Simple experiments used to reveal the behavior and characteristics of these parameters are described. A phenomenological modeling method is used to establish mathematical representations of these parameters in relation to errors such as nonlinearity, hysteresis, cross-axis effect, and temperature effect, without requiring a complete understanding of the underlying physics. Experimental results are presented, in which the physical model reduces rmse by 93.1% in comparison with the manufacturer's recommended method.

Index Terms – Accelerometer, modeling, motion-tracking.

I. INTRODUCTION

A conventional inertial measurement unit (IMU) consists of three accelerometers and three rate gyroscopes. There have been proposals for all-accelerometer IMU designs [1, 2] for applications that are cost sensitive, due to the performance superiority of low cost accelerometers relative to low cost gyros. With companies like Analog Devices leading the way, low-cost microelectromechanical systems-based (MEMS) accelerometers have gained substantial ground in inertial navigation applications in the past several years, especially in non-military and consumer markets [3, 4]. However, size and cost advantages notwithstanding, the performance of MEMS silicon accelerometers has not reached tactical or navigation grade. Testing of MEMS accelerometers on rolling artillery projectiles show that they yield an average tracking error of about 0.1g throughout a 28-second test [5]. Though the report claims that such performance is acceptable, double integration of an acceleration error of 0.1g would mean a position error of more than 350m at the end of the test.

It is this notorious integration drift that is responsible for the fact that inertial measurement technology is seldom used alone in high precision navigation or motion tracking applications. Any seemingly small error in the acceleration measurement would grow quadratically over time in the position measurement after the double integration. Therefore, to employ accelerometers effectively in high precision tracking applications, it is imperative to obtain a comprehensive model to account for the errors.

There have been some modeling efforts of MEMS capacitive accelerometers on equivalent electrical circuit models that represent the physics of operation [6, 7]. The main problem of this type of modeling is that it is not useful to a user that is merely concerned with how to use the accelerometers effectively and does not care so much about the underlying physics and low level circuitry of the sensors. More important and useful physical parameters by which accelerometers are usually rated, such as scale factor, bias, nonlinearity, cross-axis sensitivity, misalignment, noise characteristics, and temperature sensitivity are missing from these models.

For many low-g ($< 2g$) inertial sensing applications, such as indoor robotic navigation [8], motion tracking of handheld devices for microsurgery [2] and entertainment [9], etc., the signal-to-noise ratio is low and thus any unmodeled error in the aforementioned physical parameters would undermine the effectiveness of the intended application over time.

The objective of this paper is to develop a physical model of an accelerometer in order to use the accelerometer effectively, in terms of the common parameters published in the manufacturer's datasheets. Simple experiments to reveal the behavior of these parameters are described. We adopt a phenomenological modeling method to relate the experimental observations to mathematical representations of these parameters without requiring complete understanding of the underlying physics. The identified physical model is verified in a motion sensing experiment where the ground truths of the generated motion are known. The limitations of the proposed model are also discussed. While the physical model developed is specific to the accelerometer make and model tested, the experiments and modeling methodology are generic and may be used with other types of accelerometers.

II. ACCELEROMETER PHYSICS AND CONSTRUCTION

The sensor used in the development of the proposed physical model is the Analog Devices ADXL-203, a dual-axis low-g miniature MEMS-based capacitive accelerometer. The ADXL-203 measures $5\text{mm} \times 5\text{mm} \times 2\text{mm}$, weighs less than 1 gram, and has an effective sensing range of $\pm 1.5g$. It is a complete acceleration measurement system on a single monolithic integrated circuit. It contains a surface micro-machined polysilicon structure built on top of a silicon wafer, with signal conditioning circuitry to implement an open-loop acceleration measurement architecture. Polysilicon springs at

the four corners suspend the square proof mass over the surface of the wafer and provide a resistance against acceleration forces. A schematic illustration is shown in Fig. 1. Deflection of the structure due to externally applied acceleration is measured using a differential capacitor. The differential capacitor involves the interdigitation of moving fingers attached to the proof mass with independent fixed fingers attached to the base. The differential capacitance is proportional to the overlapping area and the distance between the moving and fixed fingers. With the capacitor area fixed by the manufacturing process, the differential capacitance and hence the circuit output voltage is proportional to the difference between distance d_1 and d_2 , as shown in the inset of Fig. 1. The movement of the proof mass is controlled by the suspension springs, and thus Hooke's Law applies in relating the displacement to the applied specific force. Since the modeling approach here is phenomenological, no equations of the physics of operation will be presented here. The reader is requested to refer to the datasheets and application notes from the manufacturer's website (www.analog.com) for more details. The ADXL-203 provides two output modes: analog, and digital pulse wave modulation (PWM). The former is used in our experiments, but the approaches described are also applicable to the latter.

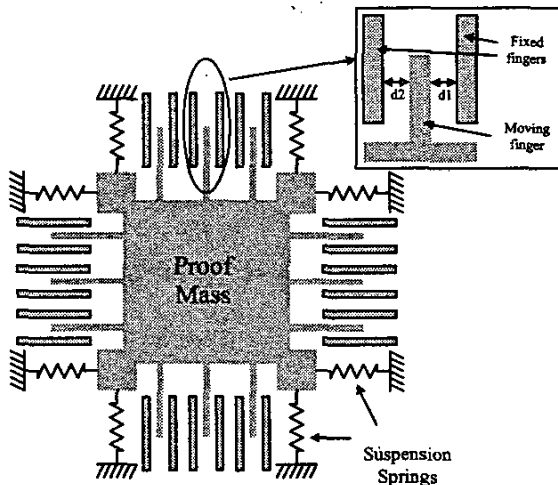


Fig. 1 Construction schematic of ADXL-203 dual-axis accelerometer.

III. SCALE FACTOR AND BIAS

Scale factor is defined as the ratio of a change in the output to a change in the input intended to be measured. It is sometimes referred to as sensitivity. Bias or zero offset is the average sensor output over a specific time measured at specified operating conditions that has no correlation with the input. The scale factor and bias are affected by factors related to material and construction, e.g., hysteresis, nonlinearity, cross-axis effects, etc., as well as factors related to operation, such as temperature and pressure.

Scale factor of an accelerometer is usually expressed in volts (V) per g , where g is the gravitational acceleration. Bias

is expressed in volts (V) or in terms of g if the scale factor is known. To determine the scale factor and bias, the manufacturer specification sheets recommend the following:

$$\text{Scale factor, } SF = (V_{+g} - V_{-g}) / 2 \text{ V/g}; \quad (1)$$

$$\text{Bias, } B = (V_{+g} + V_{-g}) / 2 \text{ V} \quad (2)$$

where V_{+g} and V_{-g} are the output of the accelerometer in volts when aligned with gravity and when aligned opposite to the direction of gravity, respectively. Thus, with accelerometer output V_o , the sensed acceleration (in terms of g) is computed as,

$$\text{Acceleration, } A = (V_o - B) / SF \text{ } g. \quad (3)$$

However, there are two problems to this approach: composite nonlinearity and temperature drift.

A. Composite Nonlinearity

The input-output relationship of the ADXL-203 accelerometer is nonlinear. The nonlinear behavior is a result of the material properties and the construction of the sensor. Two simple experiments will be performed to reveal the behavior of the accelerometer voltage output at orientations defined by two angles, α and β (see Fig. 2). The definition of the angle α is such that 0° and 180° are when the plane that contains both x- and y-sensing axes is perpendicular to the gravity plane and $\pm 90^\circ$ is where the two planes are parallel. When $\alpha = 90^\circ$, the angle β is 0° when the x-accelerometer is aligned with the gravity vector.

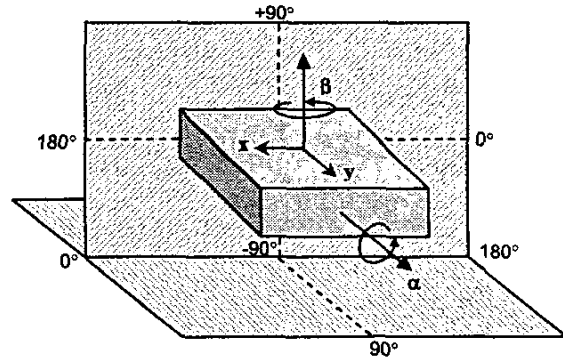


Fig. 2 Definition of angles α and β .

In the first experiment, starting with $\alpha = 90^\circ$ (see Fig. 3),

- when the accelerometer is rotated from $\beta = 0^\circ$ to 360° clockwise and anticlockwise in the gravity plane, hysteretic paths $A^+ - B^-$ and $B^+ - A^-$, respectively, are observed;
- when it is rotated clockwise and anticlockwise from $\beta = 0^\circ$ to 180° and then back to 0° in the gravity plane, paths $A^+ - A^-$ and $B^+ - B^-$, respectively, are observed.

In the second experiment, the accelerometer is inclined such that both the x- and y-sensing axes lie in a plane offset from the direction of gravity by the angle α . It is observed that

- when the accelerometer is rotated from $\beta = 0^\circ$ to 360° in the inclined plane α , there is a non-parallel upward shift of the entire hysteretic path with increasing α ;
- experiments at $\pm\alpha^\circ$ yield the same hysteretic paths.

There is no change in the accelerometer output at $\alpha = 0^\circ$ and 180° , since the sensing plane is orthogonal to gravity. For ease of illustration, only hysteretic paths $Z_{\pm 30}$, $Z_{\pm 90}$, and $Z_{\pm 150}$ are shown in Fig. 4. Note that $Z_{\pm 90}$ is the same as Fig. 3.

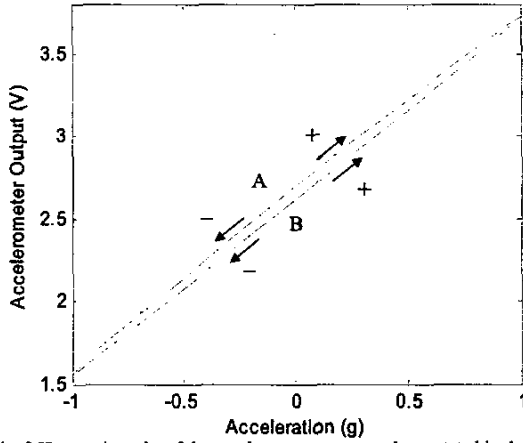


Fig. 3 Hysteretic paths of the accelerometer output when rotated in the gravity plane. When rotated clockwise and anticlockwise through 360° , it follows paths A⁺-B⁻ and B⁺-A⁻ respectively; when rotated clockwise and anticlockwise through 180° and back to 0° , it follows paths A⁺-A⁻ and B⁺-B⁻ respectively.

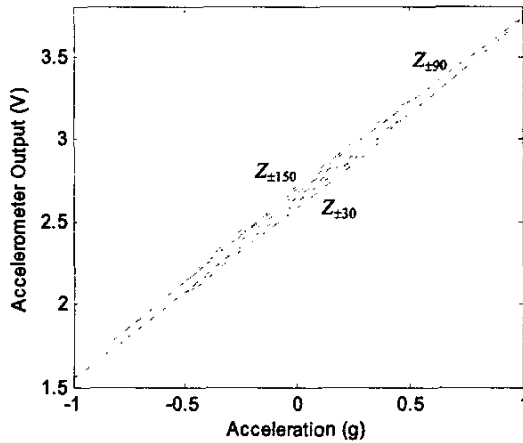


Fig. 4 Hysteretic paths of the accelerometer rotated through 360° in a plane inclined at angle $\alpha = \pm 30^\circ, \pm 90^\circ$, and $\pm 150^\circ$.

These observations are the result of composite nonlinearity errors, including material nonlinearity, hysteresis, and cross-axis effects. It is almost impossible to tell which factor contributes to which observation without specialized instrumentation. However, it is not necessary to understand the underlying physics, nor to model these errors explicitly;

there is sufficient information for us to model and compensate these errors phenomenologically.

The hysteretic behavior of the ADXL-203 accelerometer is different from the classical hysteresis found in magnetism and other shape memory alloys. One possible explanation of this observation is the cross-axis effect from the acceleration in y-axis. This is evident from the fact that, since acceleration in x- and y-sensing directions are 90° out of phase, the hysteresis error of the x-axis is largest at the point where the y-direction acceleration is the largest, and vice versa.

One probable cause of the shift of the entire hysteresis path at different inclination α is the out-of-plane cross-axis effect from the acceleration in the z direction. This is again evident from the fact that the hysteretic curves shift upward as the out-of-plane z-axis acceleration increases.

Thus, the acceleration sensed by the x-accelerometer is the combined effect of the real acceleration in the x-axis plus cross-axis accelerations from the other two orthogonal principal directions, which alter the bias and the scale factor,

$$A_x = (V_x - B_x(V_y, V_z)) / SF_x(V_z) \quad (4)$$

where V_y and V_z are respectively the output of the y-accelerometer and an external z-accelerometer. It may seem strange to include a z-accelerator output term for a dual axis accelerometer with only x- and y-sensing, but in most motion tracking applications, the IMU has three orthogonal axes of linear acceleration sensing. In a static tilt sensing application, z-accelerator output can be calculated from simple vector geometry, since the only sensed acceleration is the gravity,

$$V_z = V_g^z \sqrt{1 - \tilde{v}_x^2 - \tilde{v}_y^2}, \quad (5)$$

where \tilde{v}_x and \tilde{v}_y are normalized voltages given by

$$\tilde{v}_x = \frac{V_x}{V_g^x}, \tilde{v}_y = \frac{V_y}{V_g^y}, \quad (6)$$

$$\text{and } V_g^d = (V_{+g}^d - V_{-g}^d) / 2, \quad d = x, y, \text{ or } z, \quad (7)$$

is the output of the x-, y- or z-accelerometer in volts when aligned with gravity.

We first define a linear model $f_x(A_x)$ by rearranging (3),

$$f_x(A_x) = A_x \cdot SF_x^{90} + B_x^{90} \quad (8)$$

where SF_x^{90} and B_x^{90} are the scale factor and bias obtained from the manufacturer's recommended calibration method. The superscript "90" signifies $\alpha = 90^\circ$.

The shift in bias is a linear superposition of the cross-axis effects from the y- and z-acceleration,

$$B_x(V_y, V_z) = B_x^{90} + g_x(V_y) + h_x(V_z). \quad (9)$$

To model $g_x(V_y)$, the corresponding data generated by the linear model $f_x(A_x)$ is subtracted from the measurement data of plot $Z_{\pm 90}$ (where $h_x(V_z) = 0$),

$$R_x^j = V_{ox} - V_x \quad (10)$$

where R_x^j is the residual x-accelerometer output attributed to the effect of acceleration in y-direction, V_{ox} is the measured x-accelerometer output and V_x is the data generated by the linear model $f_x(A_x)$. R_x^j , V_{ox} , and V_x are all $n \times 1$ vectors, where n is

the number of data points. Plotting the residue vector versus the measured y-accelerometer output vector reveals that the relationship is quadratic (see Fig. 5). Hence the cross-axis effect of y-acceleration on the x-axis may be modeled by the least-squares fitting of a second-order polynomial to the data,

$$g_x(V_y) = p_{x2}V_y^2 + p_{x1}V_y + p_{x0}. \quad (11)$$

The result of this model is shown in Fig. 6.

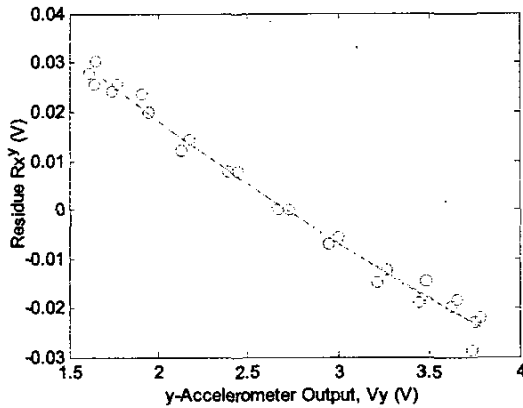


Fig. 5 The residual x-accelerometer output versus the y-accelerometer output. The relationship is quadratic.

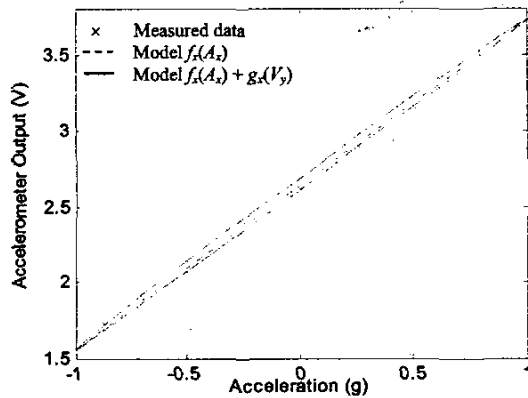


Fig. 6 The measured x-accelerometer output, the linear model $f_x(A_x)$, and the model $f_x(A_x) + g_x(V_y)$.

To model $h_x(V_z)$, we first compute the bias of the hysteretic paths generated at each inclined plane using (2) and then the difference of the bias at each α compared with that at $\alpha = 90^\circ$. Thus

$$R_x^z = B_x^\alpha - B_x^{90}, \quad (12)$$

where R_x^z is the residual x-accelerometer output attributed to the effect of acceleration in z-direction, B_x^α is the vector of the bias at each α , and B_x^{90} contains repeated values of the bias at $\alpha = 90^\circ$. They are all $m \times 1$ vectors, where m is the number of inclined planes in which we have conducted the experiment. Plotting R_x^z versus the z-accelerometer output (in this case, an analytical result based on (5) is used) shows that the

relationship is quadratic as shown in Fig. 7. Hence the cross-axis effect of z-acceleration on x-axis may be modeled by the least squares fitting of a second-order polynomial to the data,

$$h_x(V_z) = q_{x2}V_z^2 + q_{x1}V_z + q_{x0}. \quad (13)$$

The result of this model is shown in Fig. 8.

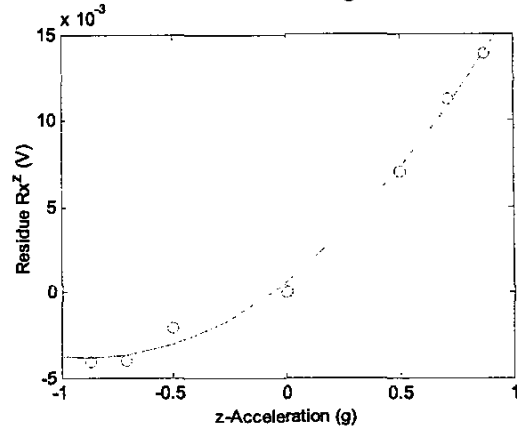


Fig. 7 The residual x-accelerometer output versus the z-acceleration. The relationship is quadratic.

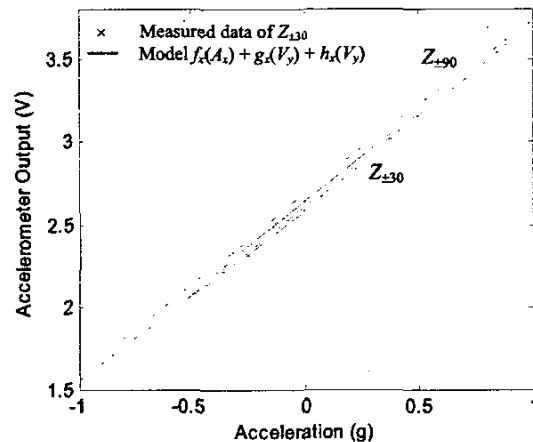


Fig. 8 The measured x-accelerometer output at $\alpha = \pm 30^\circ$ and the proposed physical model $f_x(A_x) + g_x(V_y) + h_x(V_z)$. The Z_{190} plot is added for comparison.

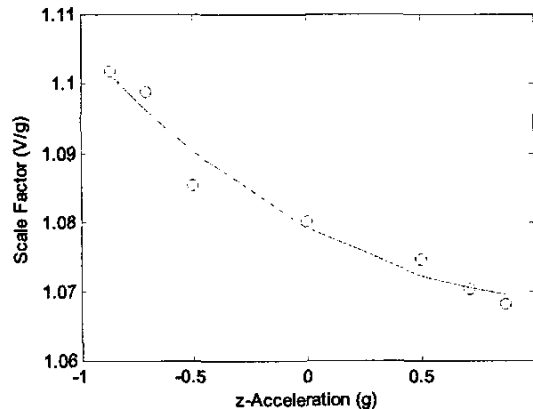


Fig. 9 Scale Factor versus z-acceleration. The relationship is quadratic.

Now we substitute (8), (11), and (13) into (4),

$$A_x = (V_x - B_x^{90} - p_{x2}V_y^2 - p_{x1}V_y - p_{x0} - q_{x2}V_z^2 - q_{x1}V_z - q_{x0})/SF_x(V_z) \quad (14)$$

where $SF_x(V_z)$ is found from the plot of SF_x versus the z-acceleration V_z as shown in Fig. 9. The scale factor model is thus

$$SF_x(V_z) = r_{x2}V_z^2 + r_{x1}V_z + r_{x0}. \quad (15)$$

The same approach is repeated to model the y-sensing axis,

$$A_y = (V_y - B_y^{90} - p_{y2}V_x^2 - p_{y1}V_x - p_{y0} - q_{y2}V_z^2 - q_{y1}V_z - q_{y0})/SF_y(V_z) \quad (16)$$

where $SF_y(V_z) = r_{y2}V_z^2 + r_{y1}V_z + r_{y0}$ (17)

B. Temperature Drift

The scale factor and bias are sensitive to temperature change. Since typical low-g motion tracking applications are generally indoors, we may assume the ambient temperature to remain constant over the operation period. However, a change in the operating temperature due to the gradual heating up of the sensor circuitry is inevitable. Fig. 10 shows the drift in the zero bias and the scale factor at different time intervals over a period of 12 hours, with a constant ambient temperature of about 22°C. We observe that in this experiment the zero bias and the scale factor drift to a steady state after about 7 hours.

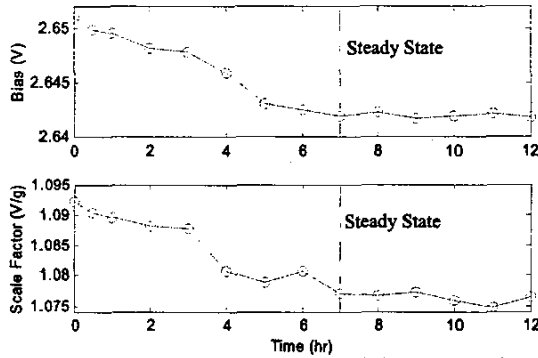


Fig. 10 Bias and scale factor temperature drift. Steady state is reached at approximately the 7th hour in this experiment.

Barshan *et al.* [8] use an exponential function to model the bias drift of two types of rate gyroscopes, and the drift model is implemented via extended Kalman filtering. To the best of the authors' knowledge there is no literature that models the scale factor drift of any type of inertial sensors. Although Barshan's approach can be easily applied with some modifications to model both the scale factor and bias of an accelerometer, it is subject to potentially large modeling error because the drift characteristics of the sensors are inconsistent between operations. Moreover, quantifying this error may involve impractically great experimental effort.

An alternate straightforward solution is to wait for the sensors' temperature drift to reach steady state, which ranges from 2 to 12 hours among the 4 accelerometers (8 sensing axes) that we have tested.

Another approach that we have tried is ovenization. A resistor is placed closed to the accelerometer to heat up and

maintain the accelerometer at a temperature higher than the ambient. Experiments have shown that steady state is reached within the first hour. However, the process changes the behavior of the accelerometer, producing higher nonlinearity and larger hysteresis. More experiments will be needed to investigate the effectiveness of this approach.

IV. MISALIGNMENT

Misalignment errors occur at both the sensor level and the system level. At the sensor level, the misalignment error refers to the x-to-y axis misalignment or the orthogonality error between the x- and y-sensing axes. At the system level, misalignment arises from machining errors of the mechanical structure on which the sensor is mounted. Since it is impossible to analyze the latter in general, we select two reference surfaces or edges of the accelerometer and assume that the corresponding matching surfaces on the mounting structure are machined to a good tolerance. Therefore, we model the system level misalignment errors of the sensing axes with respect to this two reference surfaces or edges.

The flat square surface without the connection pins and one of the sides parallel to the x-sensing axis are chosen to be the references. We define the normal to the reference surface z_{ref} , the reference edge x_{ref} , and y_{ref} as the imaginary vector that completes the right hand coordinate system. The accelerometer is mounted with the reference surface aligned with the gravity plane and the reference edge parallel to the gravity vector. We rotate the accelerometer about y_{ref} by α° and then about z_{ref} by β° until a maximum (or minimum if x_{ref} is aligned with $-g$) x-output voltage is registered. The orientation of the real x-sensing axis with respect to the reference frame xyz_{ref} is then found by

$$\Theta_x = R_y(\alpha_x)R_z(\beta_x)x_{ref} = [\theta_{xx} \ \theta_{xy} \ \theta_{xz}]^T \quad (18)$$

where $R_y(\alpha_x)$ and $R_z(\beta_x)$ are 3x3 rotation matrix about y_{ref} and z_{ref} respectively, with $x_{ref} = [0 \ 0 \ 1]^T$. For the y-sensing axis, we rotate the accelerometer by 90° about z_{ref} and repeat the same experiment to find α_y and β_y , then with $y_{ref} = [0 \ 1 \ 0]^T$,

$$\Theta_y = R_x(\alpha_y)R_z(\beta_y)y_{ref} = [\theta_{yx} \ \theta_{yy} \ \theta_{yz}]^T. \quad (19)$$

The x- and y-accelerations obtained from (14) – (17) are sensed along directions Θ_x and Θ_y respectively. The accelerations along the reference axes may be computed as

$$A_{xref} \approx (A_x - \theta_{yx}A_y - \theta_{xz}A_z)/\theta_{xx} \quad (20)$$

$$A_{yref} \approx (A_y - \theta_{yx}A_{xref} - \theta_{yz}A_z)/\theta_{yy}. \quad (21)$$

Note that (20) uses uncorrected A_x and A_z , while (21) uses the corrected A_{xref} and uncorrected A_z . This would be a good approximation since θ_{ij} , $i \neq j$, are typically small. In our experiment, $\alpha_x = 0.75^\circ$, $\beta_x = -0.33^\circ$, $\Theta_x = [0.9999 \ -0.0058 \ -0.0131]^T$ and $\alpha_y = 0.75^\circ$, $\beta_y = 0.5^\circ$, $\Theta_y = [-0.0029 \ 0.9999 \ 0.0131]^T$. The α 's and β 's are measured to an accuracy of $\pm 0.2^\circ$.

V. EXPERIMENTAL SETUP

All the experiments described in the previous sections are performed on an experimental setup made of two orthogonal precision rotary stages with resolution of 0.083° (5 arcmin). A capacitor of $0.33\mu\text{F}$ is connected respectively between the x- and y-axis analog outputs and the signal ground, which combines with the sensor output impedance of $32\text{ k}\Omega$ to become a simple first order R-C low-pass filter with cut-off frequency at around 15.2 Hz . The sensor output is sampled at 1 kHz by a 16-bit analog-to-digital converter. The inclinations of the rotary stages are checked prior to each experiment by a digital level with a resolution of 0.1° . The noise floor of the sensor analog outputs is about 3.1 mV p-p , which is computed from 4 times the measured rms noise, the upper limit of the peak-to-peak noise 95.4% of the time, as specified in the datasheet. This would correspond to a minimum perceivable inclination change of approximately 0.2° . This means that experimental errors due to human inconsistency and parallax error in the order of 0.01° are negligible compared to the noise floor. Because of the stochastic nature of the sensor output, the mean of 5 seconds worth of data (5000 data points) is used in these experiments.

The motion sensing experiment consists of a motion generator and a displacement sensor. The motion generator is a 3-axis piezo-driven linear nano-positioner (Polytec-PI, Inc., Model P-611) and the motion sensor is an infrared interferometer (Philtec, Inc., Model D63) with sub-micrometer resolution. An ADXL-203 accelerometer is mounted on top of the motion generator with its reference edges aligned with the edges of the motion generator. The motion generator is mounted on the rotary stages with an inclination of $\alpha = +45^\circ$, and rotated to $\beta = +90^\circ$ as shown in Fig. 11. The motion generator generates an oscillation of $60\text{ }\mu\text{m p-p}$ at 10 Hz in the x-sensing direction, which is perpendicular to the gravity vector. The interferometer is placed in front of the motion generator aligned with the x-direction to measure the displacement profile of the motion generator. The interferometer is sampled at 1 kHz .

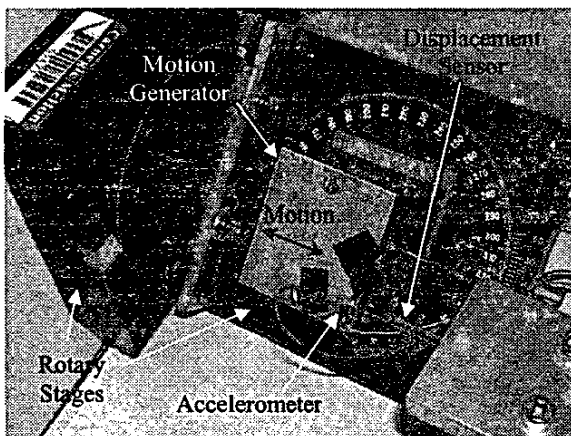


Fig. 11 Motion sensing experiment setup.

VI. RESULTS

The data collected by the interferometer is low-pass filtered with a second-order digital Butterworth filter with cut-off frequency at 20 Hz . It is then corrected for phase shift and attenuation before being differentiated twice to obtain the acceleration profile of the motion generator. The accelerometer voltage output is also corrected for phase shift and attenuation due to the analog R-C low-pass filter and then converted to acceleration in mm/s^2 based on both the manufacturer's recommended linear model, (1) – (3), and the proposed physical model, (4) – (21). The gravity constant g used is 9801.31 mm/s^2 , computed based on the latitude and altitude of our laboratory.

Fig. 12(a) shows the plot of the acceleration profile sensed by the interferometer and that from the accelerometer based on the linear model. The rmse is 299.8 mm/s^2 , most of which is the result of the shift in bias. Fig. 12(b) shows the same interferometer acceleration plot and that computed by the proposed physical model. The physical model eliminates most of the bias shift error. The rmse is 20.8 mm/s^2 , an improvement of 93.1% over the linear model.

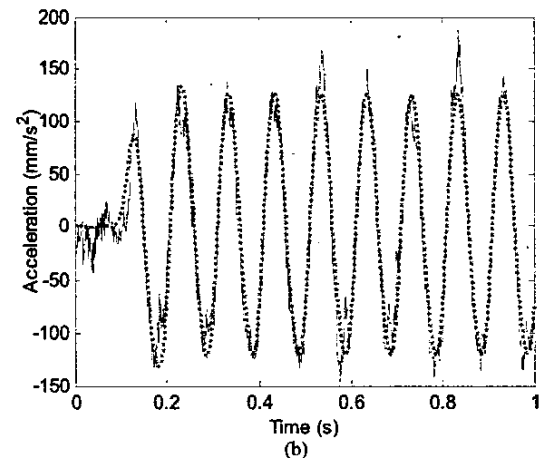
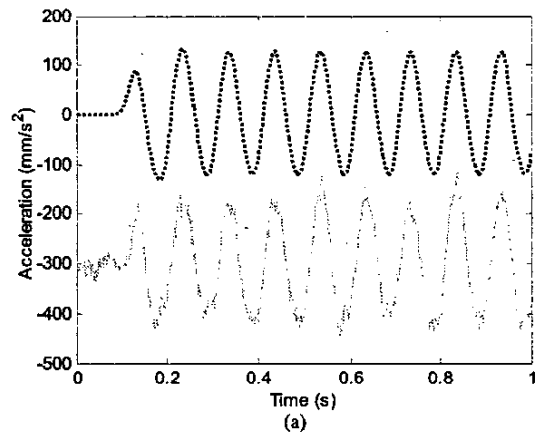


Fig. 12 Results of (a) the manufacturer's recommended linear model vs (b) the proposed physical model. The dotted line is the computed acceleration from the interferometer. The solid line is the measured acceleration from the x-accelerometer.

VII. DISCUSSION

The proposed physical model performed well compared to the manufacturer's recommended linear model as described by (3). The action of each component of the physical model is depicted in Fig. 13. The accelerometer is first calibrated at $\alpha = +90^\circ$, which gives the line labeled 'Linear Model'. For the motion sensing experiment, the accelerometer is rotated to $\alpha = +45^\circ$ and $\beta = +90^\circ$ at which its response to acceleration in x is represented by the line labeled 'Actual Response'. With the output voltage V_x , the linear model indicates an acceleration of A_x' . The difference between the actual acceleration A_x and A_x' results in the offset observed in Fig. 12(a). The model $B_x(V_x, V_z)$ shifts the linear model parallel toward the actual response and the model $SF_x(V_z)$ alters the gradient and result in the line ' $B_x + SF_x$ '. Correction for the misalignment vector Θ_x makes the final shift of the line toward the actual response, which gives the plot in Fig. 12(b).

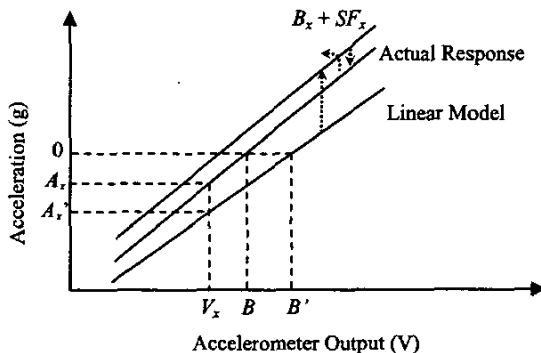


Fig. 13 The action of each component of the physical model on the accelerometer response plot. The line 'Linear Model' is obtained from the manufacturer's recommended calibration method. The bias model $B_x(V_x, V_z)$ shifts the linear model parallel towards the actual response and the model $SF_x(V_z)$ alters the gradient and result in the line ' $B_x + SF_x$ '. The misalignment model makes the final shift to the line 'Actual Response'.

The main contribution of this paper is the development of a physical model of a dual-axis MEMS accelerometer that is based solely on experimental observations. With the intended application of low signal-to-noise ratio motion tracking scenarios in mind, the proposed physical model includes only the physical parameters that matter to an end user of the accelerometer. The strength of this phenomenological approach of modeling the scale factor, bias, and misalignment is that errors such as nonlinearity, hysteresis, cross-axis effects, and temperature drift are captured with very simple experiments without the need to understand the underlying physics.

The accuracy of the proposed physical model is limited by the stochasticity and inconsistent behavior of the accelerometer between operations. The random noise makes it difficult to model the misalignment accurately. In applications like our motion sensing experiment, in which the acceleration

to be sensed is about two orders of magnitude smaller than g , small orientation error in the sensing axes will result in a gravity residue comparable to the motion acceleration. The variation of the temperature drift pattern handicaps the usefulness of modeling the drift. While the practicality of ovenization is still under investigation, waiting for the accelerometer to reach its steady state seems to be the most robust solution.

VIII. CONCLUSION

A physical model of a dual-axis MEMS accelerometer intended for low- g motion tracking applications has been proposed. The model is based on phenomenological modeling of the physical parameters that an accelerometer is commonly rated: scale factor, bias, and misalignment. The model captures the errors in these parameters due to nonlinearity, hysteresis, cross-axis effects, and temperature drift. In a motion sensing experiment, the proposed model outperforms the manufacturer's recommended linear model by 93.1% in terms of rmse of the sensed acceleration.

REFERENCES

- [1] J. H. Chen, S. C. Lee, D. B. DeBra, "Gyroscope Free Strapdown Inertial Measurement Unit by Six Linear Accelerometers", *Journal of Guidance, Control, and Dynamics*, Vol.17, No.2, March-April 1994, pp.286-290.
- [2] W. T. Ang, P. K. Khosla, and C. N. Riviere, "Design of All-Accelerometer Inertial Measurement Unit for Tremor Sensing in Handheld Microsurgical Instrument," *Proc. IEEE Intl. Conf. Rob. and Auto.*, pp.1781-1786, Sep 2003.
- [3] N. Barbour and G. Schmidt, "Inertial Sensor Technology Trends," *IEEE Sensors Journal*, vol.1, No. 4, pp. 332-339, Dec 2001.
- [4] J. L. Weston and D. H. Titterton, "Modern Inertial Navigation Technology and its Application," *Electronics & Comm. Eng. Journal*, pp.49-64, April 2000.
- [5] B. S. Davis, "Using Low-Cost MEMS Accelerometers and Gyroscopes as Strapdown IMUs on Rolling Projectiles," *Proc. Position Location and Navigation Symp.*, pp.594-601, Apr. 1998.
- [6] W. F. Lee, P. K. Chan, and L. Siek, "Electrical Modeling of MEMS Sensors for Integrated Accelerometer Applications," *Proc. Electron Devices Meeting*, pp.88-91, June 1999.
- [7] C. Bourgeois, F. Porrent, and A. Hoogerwerf, "Analytical Modeling of Squeeze-Film Damping in Accelerometers", *Proc. IEEE Int'l Conf. Solid-State Sensors and Actuators*, pp. 1117-1120, June 1997.
- [8] B. Barshan and H. F. Durrant-Whyte, "Inertial Navigation Systems for Mobile Robots", *IEEE Trans. On Robotics and Automation*, Vol.11, No.3, pp. 328-342, Feb 1994.
- [9] C. Verplaetse, "Inertial proprioceptive devices: Self-motion-sensing toys and tools," *IBM Systems Journal*, Vol.35, Nos. 3 & 4, pp.639-650, 1996.